The influence of fiber dispersion on the mechanical response of aortic tissues in health and disease: A computational study

Justyna A. Niestrawska[a], Daniel Haspinger[a] and Gerhard A. Holzapfel[a,b,1]

[a] Institute of Biomechanics, Graz University of Technology
Stremayrgasse 16/2, 8010 Graz, Austria

[b] Norwegian University of Science and Technology (NTNU)
Faculty of Engineering Science and Technology, 7491 Trondheim, Norway

Abstract. Changes in the structural components of aortic tissues have been shown to play a significant role in the pathogenesis of aortic degeneration. Therefore, reliable stress analyses require a suitable and meaningful constitutive model that captures micro-structural changes. As recent data show, in-plane and out-of-plane collagen fiber dispersions vary significantly between healthy and aneurysmatic aortic walls. The aim of this study is to computationally investigate the influence of fiber dispersion on the mechanical response of aortic tissues in health and disease. In particular, the influence of three different fiber dispersions is studied: (i) non-rotationally symmetric dispersion, the most realistic assumption for aortic tissues; (ii) transversely isotropic dispersion, a special case; (iii) perfectly aligned fibers (no dispersion in either plane), another special case. Explicit expressions for the stress and elasticity tensors as needed for the implementation in a finite element code are provided. Three representative numerical examples are studied: planar biaxial extension, inflation of residually stressed and pre-stretched aortic segments and inflation of an idealized abdominal aortic aneurysm (AAA) geometry. For the AAA geometry the case of isotropic dispersion is additionally analyzed. Documented structural and mechanical parameters are taken from human aortas (healthy media/adventitia and AAA). The influence of fiber dispersions upon magnitudes and distributions of stresses and deformations are presented and analyzed. Stresses vary significantly, especially in the AAA case, where material stiffening is significantly influenced by fiber dispersion. The results highlight the need to incorporate the structural differences into finite element simulations to obtain more accurate stress predictions. Additionally, results show the capability of one constitutive model to represent different scenarios of aortic micro-structures allowing future studies of collagen reorientation during disease progression.

Keywords: Collagen fiber dispersion, constitutive model, arterial wall mechanics, human aorta, abdominal aortic aneurysm, finite element method

---

[1]To whom correspondence should be addressed. Email address: `holzapfel@tugraz.at`

1 Introduction

Aortic tissues can be viewed as fibrous composites assembled from a ground matrix and embedded families of collagen fibers with orientations that are distributed spatially. It is well established that the mechanical behavior of fibrous tissues such as arterial walls is strongly influenced by the underlying collagen structure, in particular, by collagen orientation *and* dispersion, see, e.g., Holzapfel and Ogden [1]. It has been shown that during the development of diseases such as an abdominal aortic aneurysm (AAA) the collagen structure changes significantly. For example, collagen fibers in healthy abdominal aortas are considerably dispersed in-plane (circumferential-axial plane), but have a rather small dispersion out-of-plane (circumferential-radial plane) (Schriefl et al. [2]; Niestrawska et al. [3]). AAAs, however, show a significantly higher dispersion out-of-plane. In addition, by means of several samples it has been shown that the characteristic three-layered wall structure, as seen in healthy abdominal aortas, is no longer present in AAAs [3]. A quantification and analysis of the reorientation of the micro-structure are key to better understand disease progression. The recently proposed model by Holzapfel et al. [4] is one that is able to capture the spatially distributed orientations of collagen fibers in arterial tissues, and, therefore, allows to provide a deeper insight into the (pathological) changes of fibrous tissues as occurring in AAAs.

As mentioned, the mechanical response of aortic tissues is strongly influenced by the underlying collagen structure. Nevertheless, several studies which investigate the magnitude and location of peak wall stresses in AAAs have utilized either isotropic models (see, e.g. Elger et al. [5]; Vorp et al. [6]; Raghavan et al. [7]; Raghavan and Vorp et al. [8]; Thubrikar et al. [9]; Doyle et al. [10]; Raut et al. [11]) or material parameters which were received from healthy aortic tissues (Pierce et al. [12]). Early studies have used the law of Laplace to study the influence of the geometry on AAA stresses (Stringfellow et al. [13]; McGiffin et al. [14]) or modeled AAAs as axisymmetric membranes (Elger et al. [5]). Also linear elastic models were used to study AAA stresses (Inzoli et al. [15]; Mower et al. [16]); these models are not able to capture the typical nonlinear behavior of aortic tissues. Studies such as those by Vande Geest et al. [17], Tong et al. [18], O'Leary et al. [19], Sassani et al. [20] or Niestrawska et al. [3] have illustrated that AAA tissues are anisotropic, which requires the consideration of appropriate models and parameters to analysis wall stresses. Especially as three-dimensional (3D) imaging data of the wall micro-structure become available it should be combined with mechanical data to ensure more accurate estimates of wall stress magnitudes and related locations.

The influence of material parameters and models on wall stress predictions was studied by several groups, with contradicting results. While the studies by Raghavan and Vorp [8] and

Fillinger et al. [21, 22] stated that the peak wall stress is mainly influenced by AAA shape and/or AAA diameter, Polzer et al. [23] stated that it is important to account for nonlinearity when simulating AAA responses. On the basis of the same AAA geometry Rodríguez et al. [24] showed that the use of an anisotropic model yields higher maximum wall stresses when compared with isotropic models. The same group investigated the influence of anisotropy on peak wall stresses. They also studied the impact of the model on five different patient-specific AAA geometries and concluded that the inclusion of anisotropy scales up the magnitude of peak wall stresses (Rodríguez et al. [25]). Additionally they studied the outcome of two different anisotropic models, one of them was the model by Holzapfel et al. [26] and the other one by Rodríguez et al. [24], and they concluded that parameters describing the fiber orientation should always be obtained independently from the fitting of the other parameters to stress-strain data. However, the authors fitted the models they compared to different data sets, hence their conclusion on the influence of fiber dispersion is not that compelling.

To the authors' knowledge the influence of different fiber dispersions on the basis of the structural model by Holzapfel et al. [4] using systematic numerical simulations has not yet been studied. In addition, stress distributions obtained from parameter sets taken from healthy and diseased aortic tissues have not yet been compared. The present paper aims to investigate the influence of three different fiber dispersions: (i) non-rotationally symmetric dispersion, which is the most realistic assumption recently introduced by Holzapfel et al. [4]; (ii) transversely isotropic (rotationally symmetric) dispersion, according to Gasser et al. [27], a special case of [4]; (iii) perfectly aligned fibers (no dispersion in either plane), according to Holzapfel et al. [26], another special case of [4]. All three dispersion assumptions are studied with material and structural parameters obtained from the media and adventitia of healthy abdominal aortic walls, and from one AAA sample (Niestrawska et al. [3]).

The outline of the paper is as follows. In Section 2 the required continuum mechanical framework is provided by briefly explaining the utilized non-symmetric fiber dispersion model [4]. In addition, explicit expressions for the stress and elasticity tensors are provided, as needed for the implementation in a finite element code. In Section 3 the used method is described, i.e. different fiber dispersions are studied using three representative numerical examples, and related finite element simulations are performed. The results of these simulations are then summarized and discussed in Section 4, which is followed by a conclusion.

2   Continuum Mechanical Framework

This section briefly reviews the required continuum mechanical framework, with notation according to Holzapfel [28], and summarizes the used non-symmetric (non-rotationally symmetric) fiber dispersion model. It provides the background for the mathematical description of the stress and elasticity tensors needed for the implementation in the general purpose finite element analysis program FEAP (Taylor [29]).

2.1   Kinematics

Let Ω_0 be a reference (or undeformed) configuration and Ω its current (or deformed) configuration. The deformation map $\boldsymbol{\chi}(\mathbf{X})$ transforms a material point $\mathbf{X} \in \Omega_0$ into a spatial point $\mathbf{x} \in \Omega$. With this map we define the deformation gradient $\mathbf{F} = \partial \boldsymbol{\chi}(\mathbf{X})/\partial \mathbf{X}$ that allows to map a tangent vector $\mathrm{d}\mathbf{X}$ from the reference to the current configuration via $\mathrm{d}\mathbf{x} = \mathbf{F}\mathrm{d}\mathbf{X}$. The determinant of $\mathbf{F}$ is denoted by J and describes the ratio between the volume in the current and the reference configuration. For incompressible materials, as considered in the present work, J requires to be equal to unity (Holzapfel [28]). For subsequent use we decouple $\mathbf{F}$ into a spherical (dilatational) part $J^{1/3}\mathbf{I}$ and a unimodular (distortional) part $\overline{\mathbf{F}} = J^{-1/3}\mathbf{F}$, with $\det\overline{\mathbf{F}} \equiv 1$; the second-order unit tensor is denoted by $\mathbf{I}$. The right Cauchy–Green tensor $\mathbf{C} = \mathbf{F}^{\mathrm{T}}\mathbf{F}$ and the left Cauchy–Green tensor $\mathbf{b} = \mathbf{F}\mathbf{F}^{\mathrm{T}}$ are defined together with their modified counterparts $\overline{\mathbf{C}} = \overline{\mathbf{F}}^{\mathrm{T}}\overline{\mathbf{F}}$ and $\overline{\mathbf{b}} = \overline{\mathbf{F}}\,\overline{\mathbf{F}}^{\mathrm{T}}$, respectively, with the related invariants $I_1 = \mathrm{tr}\mathbf{C} = \mathrm{tr}\mathbf{b}$ and $\bar{I}_1 = \mathrm{tr}\overline{\mathbf{C}} = \mathrm{tr}\overline{\mathbf{b}}$.

2.2   Non-symmetric fiber dispersion model

Let us now introduce the probability density $\rho(\Theta, \Phi)$ of the (collagen) fiber orientation in the reference configuration in terms of the two angles Θ and Φ (Holzapfel et al. [4]). The experimentally observed distribution of the collagen fibers in the aorta is non-symmetric [2, 3] so that we decompose ρ in the form $\rho(\Theta, \Phi) = \rho_{\mathrm{ip}}(\Phi)\rho_{\mathrm{op}}(\Theta)$, where $\rho_{\mathrm{ip}}(\Phi)$ and $\rho_{\mathrm{op}}(\Theta)$ describe the in-plane and out-of-plane dispersions, respectively. For ρ_{ip} and ρ_{op} we consider the von Mises distributions of the forms

$$\rho_{\mathrm{ip}}(\Phi) = \frac{\exp[a\cos 2(\Phi \pm \alpha)]}{I_0(a)}, \qquad \rho_{\mathrm{op}}(\Theta) = 2\sqrt{\frac{2b}{\pi}}\frac{\exp[b(\cos 2\Theta - 1)]}{\mathrm{erf}(\sqrt{2b})}, \qquad (1)$$

where a and b are constant concentration parameters, $I_0(a)$ is the modified Bessel function of the first kind of order 0, and α denotes the angle between the mean fiber direction and the circumferential direction of the blood vessel. To include the fiber dispersion into a strain-energy

4

function, two scalar measures can be defined according to [4], namely

$$\kappa_{\text{ip}} = \frac{1}{2} - \frac{I_1(a)}{2I_0(a)}, \qquad \kappa_{\text{op}} = \frac{1}{2} - \frac{1}{8b} + \frac{1}{4}\sqrt{\frac{2}{\pi b}}\frac{\exp(-2b)}{\text{erf}(\sqrt{2b})}, \tag{2}$$

where $I_1(a)$ is the modified Bessel function of the first kind of order 1, and $0 \leq \kappa_{\text{ip}} \leq 1$ and $0 \leq \kappa_{\text{op}} \leq 1/2$.

We introduce now two symmetric fiber families with the (in-plane) mean fiber directions

$$\mathbf{M}_4 = \cos\alpha\mathbf{e}_1 + \sin\alpha\mathbf{e}_2, \qquad \mathbf{M}_6 = \cos\alpha\mathbf{e}_1 - \sin\alpha\mathbf{e}_2, \tag{3}$$

where $\mathbf{e}_1$ denotes the circumferential direction and $\mathbf{e}_2$ the axial direction of the blood vessel. Additionally, we introduce the invariants I_4, I_6 and I_{n}, i.e.

$$I_i = \mathbf{C} : \mathbf{M}_i \otimes \mathbf{M}_i, \quad i = 4, 6, \qquad I_{\text{n}} = \mathbf{C} : \mathbf{M}_{\text{n}} \otimes \mathbf{M}_{\text{n}}, \tag{4}$$

where $\mathbf{M}_{\text{n}}$ is a unit out-of-plane vector. The related modified invariants are simply $\bar{I}_i = J^{-2/3}I_i$ and $\bar{I}_{\text{n}} = J^{-2/3}I_{\text{n}}$.

To include the fiber dispersion in the strain-energy function, say Ψ, the generalized structure tensors $\mathbf{H}_4$ and $\mathbf{H}_6$, describing the material behavior, are then used, i.e.

$$\mathbf{H}_i = A\mathbf{I} + B\mathbf{M}_i \otimes \mathbf{M}_i + (1 - 3A - B)\mathbf{M}_{\text{n}} \otimes \mathbf{M}_{\text{n}}, \qquad i = 4, 6, \tag{5}$$

with the constants

$$A = 2\kappa_{\text{op}}\kappa_{\text{ip}}, \qquad B = 2\kappa_{\text{op}}(1 - 2\kappa_{\text{ip}}). \tag{6}$$

According to [28] the strain-energy function Ψ (per unit reference volume) is now additively decomposed into Ψ_{vol}, describing the volumetric elastic response, and $\overline{\Psi}$ describing the isochoric elastic response. Thus,

$$\Psi = \Psi_{\text{vol}}(J) + \overline{\Psi}(\overline{\mathbf{C}}, \mathbf{H}_4, \mathbf{H}_6), \tag{7}$$

where $\Psi_{\text{vol}} = \bar{\kappa}(\ln J)^2/2$ serves here as a penalty function, and $\bar{\kappa}$ is a (positive) penalty parameter (for the subsequent analyses we used $10\,000\,\text{kPa}$). The isochoric part $\overline{\Psi}$ of Ψ has now the form

$$\overline{\Psi} = \Psi_{\text{g}}(\overline{\mathbf{C}}) + \sum_{i=4,6} \Psi_{\text{f},i}(\overline{\mathbf{C}}, \mathbf{H}_i), \tag{8}$$

where

$$\Psi_{\text{g}}(\overline{\mathbf{C}}) = \frac{c}{2}(\bar{I}_1 - 3) \tag{9}$$

captures the energy stored in the ground matrix, with c representing the stiffness of the (non-collageneous) matrix, and the contribution $\Psi_{\text{f},i}$ of the two fiber families is captured by

$$\Psi_{\text{f},i}\left(\overline{\mathbf{C}}, \mathbf{H}_i\right) = \frac{k_1}{2k_2}[\exp(k_2\overline{E}_i^2) - 1], \qquad i = 4, 6, \tag{10}$$

where $k_1 > 0$ is a stress-like parameter and $k_2 > 0$ is a dimensionless parameter, while $\overline{E}_i$ are quantities according to

$$\overline{E}_i = \mathrm{tr}(\mathbf{H}_i\overline{\mathbf{C}}) - 1 = A\bar{I}_1 + B\bar{I}_i + (1 - 3A - B)\bar{I}_{\mathrm{n}} - 1, \qquad i = 4, 6. \tag{11}$$

In (11) the mean fiber directions $\mathbf{M}_i$ are included in form of the invariants $\bar{I}_i$, while the dispersion parameters κ_{ip} and κ_{op} are considered in the constants A and B.

2.2.1 Stress tensors

The second Piola-Kirchhoff stress tensor $\mathbf{S}$ describes the change of the strain energy with respect to $\mathbf{C}$ and is defined by $\mathbf{S} = 2\partial\Psi/\partial\mathbf{C}$. Using the introduced decoupled form of the strain-energy function (7) two stress contributions can be identified such that $\mathbf{S} = \mathbf{S}_{\mathrm{vol}} + \overline{\mathbf{S}}$. The volumetric part is derived by means of the chain rule, which reads

$$\mathbf{S}_{\mathrm{vol}} = 2\frac{\partial\Psi_{\mathrm{vol}}(J)}{\partial J}\frac{\partial J}{\partial\mathbf{C}} = pJ\mathbf{C}^{-1}, \qquad p = \frac{\mathrm{d}\Psi_{\mathrm{vol}}(J)}{\mathrm{d}J}, \tag{12}$$

where p denotes the hydrostatic pressure. The isochoric contribution to $\mathbf{S}$ is obtained by

$$\overline{\mathbf{S}} = 2\frac{\partial\overline{\Psi}}{\partial\mathbf{C}} = J^{-2/3}\mathbb{P} : \tilde{\mathbf{S}}, \qquad \tilde{\mathbf{S}} = 2\frac{\partial\overline{\Psi}}{\partial\overline{\mathbf{C}}}, \tag{13}$$

where $\mathbb{P} = \mathbb{I} - \frac{1}{3}\mathbf{C}^{-1} \otimes \mathbf{C}$ is the projection tensor in the Lagrangian setting, $\mathbb{I}$ is the fourth-order identity tensor and $\tilde{\mathbf{S}}$ is the fictitious second Piola-Kirchhoff stress tensor. According to the introduced structure of the strain-energy function (8) we may write $\tilde{\mathbf{S}}$ as

$$\tilde{\mathbf{S}} = \tilde{\mathbf{S}}_{\mathrm{g}} + \sum_{i=4,6} \tilde{\mathbf{S}}_{\mathrm{f},i}, \qquad \tilde{\mathbf{S}}_{\mathrm{g}} = 2\frac{\partial\Psi_{\mathrm{g}}}{\partial\overline{\mathbf{C}}} = c\mathbf{I}, \quad \tilde{\mathbf{S}}_{\mathrm{f},i} = 2\frac{\partial\Psi_{\mathrm{f},i}}{\partial\overline{\mathbf{C}}} = 2\psi_i'\mathbf{H}_i, \tag{14}$$

where (9)-(11) and the abbreviation

$$\psi_i' = \frac{\partial\Psi_{\mathrm{f},i}}{\partial\overline{E}_i} = k_1\overline{E}_i\exp(k_2\overline{E}_i^2) \tag{15}$$

have been used.

For the finite element implementation we use the Kirchhoff stress tensor $\boldsymbol{\tau}$, which is the push forward of $\mathbf{S}$ so that

$$\boldsymbol{\tau} = \mathbf{FSF}^{\mathrm{T}} = \boldsymbol{\tau}_{\mathrm{vol}} + \overline{\boldsymbol{\tau}}, \tag{16}$$

where

$$\boldsymbol{\tau}_{\mathrm{vol}} = pJ\mathbf{I}, \qquad \overline{\boldsymbol{\tau}} = \mathbb{P} : \tilde{\boldsymbol{\tau}}, \tag{17}$$

$\mathbb{P} = \mathbb{I} - \frac{1}{3}\mathbf{I} \otimes \mathbf{I}$ is the projection tensor (deviatoric operator) in the Eulerian description, and $\tilde{\boldsymbol{\tau}}$ is the push forward of the fictitious second Piola-Kirchhoff tensor given in eq. $(13)_2$. The contributions of the ground matrix and the fibers to the fictitious stress can be split according to

$$\tilde{\boldsymbol{\tau}} = \tilde{\boldsymbol{\tau}}_{\mathrm{g}} + \sum_{i=4,6} \tilde{\boldsymbol{\tau}}_{\mathrm{f},i}, \tag{18}$$

which is the analogue of eq. $(14)_1$. Hence, from $(14)_2$ and $(14)_3$ we get the fictitious Kirchhoff stress tensors by a push-forward operation according to

$$\tilde{\boldsymbol{\tau}}_{\mathrm{g}} = \overline{\mathbf{F}}\tilde{\mathbf{S}}_{\mathrm{g}}\overline{\mathbf{F}}^{\mathrm{T}} = c\overline{\mathbf{b}}, \qquad \tilde{\boldsymbol{\tau}}_{\mathrm{f},i} = \overline{\mathbf{F}}\tilde{\mathbf{S}}_{\mathrm{f},i}\overline{\mathbf{F}}^{\mathrm{T}} = 2\psi_i'\overline{\mathbf{h}}_i, \tag{19}$$

where the definition for the Eulerian structure tensors

$$\overline{\mathbf{h}}_i = \overline{\mathbf{F}}\mathbf{H}_i\overline{\mathbf{F}}^{\mathrm{T}}, \qquad i = 4, 6, \tag{20}$$

has been introduced.

2.2.2 Elasticity tensors

The decoupled form of the Eulerian elasticity tensor $\mathbb{C}$ can be obtained in an analogous manner as the decoupled stress tensor $(16)_2$, i.e.

$$\mathbb{C} = \mathbb{C}_{\mathrm{vol}} + \overline{\mathbb{C}}, \tag{21}$$

with $\mathbb{C}_{\mathrm{vol}} = \tilde{p}\mathbf{I} \otimes \mathbf{I} - 2p\mathbb{I}$, where $\tilde{p} = p + J\mathrm{d}p/\mathrm{d}J$, and [28]

$$J\overline{\mathbb{C}} = \mathbb{P} : \tilde{\mathbb{C}} : \mathbb{P} + \frac{2}{3}\mathrm{tr}(\tilde{\boldsymbol{\tau}})\mathbb{P} - \frac{2}{3}(\mathbf{I} \otimes \overline{\boldsymbol{\tau}} + \overline{\boldsymbol{\tau}} \otimes \mathbf{I}), \tag{22}$$

where $\tilde{\mathbb{C}}$ is the fourth-order fictitious elasticity tensor in the Eulerian description, defined as the push-forward operation of $2J^{-4/3}\partial\tilde{\mathbf{S}}/\partial\overline{\mathbf{C}}$. By using the specific choice of the strain-energy function and the derived stress relation (14) for $\tilde{\mathbb{C}}$ we obtain the explicit form

$$\tilde{\mathbb{C}} = 4J^{-4/3}\psi_i''\overline{\mathbf{h}}_i \otimes \overline{\mathbf{h}}_i, \tag{23}$$

where the definition (20) and the abbreviation

$$\psi_i'' = \frac{\partial^2 \Psi_{\mathrm{f},i}}{\partial\overline{E}_i^2} = k_1(1 + 2k_2\overline{E}_i^2)\exp(k_2\overline{E}_i^2) \tag{24}$$

have been used. Hence, with (23), (20) and the stress tensors (18) and $(17)_2$ the purely isochoric contribution $\overline{\mathbb{C}}$ to the Eulerian elasticity tensor can be calculated from relationship (22).

By considering minor and major symmetries of the elasticity tensors the Voigt notation was then used for the implementation in the finite element analysis program FEAP [29].

3 Methods

Here we describe three cases of fiber dispersions. The (material and structural) parameters used for the numerical analyses of three examples are outlined in detail.

3.1 Parameters used for the numerical analyses

We are studying three different cases of fiber dispersions:

(i) Non-rotationally symmetric dispersion (i.e. the general case), as introduced in 2015, and reviewed in Section 2; for more details see Holzapfel et al. [4]. We refer to this case as NRSD (**n**on-**r**otationally **s**ymmetric **d**ispersion).

(ii) Transversely isotropic (rotationally symmetric) dispersion, as introduced in the GOH model in 2006, see Gasser et al. [27]. For this case the structure tensors (5) have the special form

$$\mathbf{H}_i = \kappa \mathbf{I} + (1 - 3\kappa)\mathbf{M}_i \otimes \mathbf{M}_i, \tag{25}$$

where $\kappa \in [0, 1/3]$ is a single dispersion parameter. Equation (25) is obtained from (5) by taking $\kappa = 1 - 2\kappa_{\mathrm{op}}$, which corresponds to $A = \kappa$, $B = 1 - 3\kappa$. We refer to this special case as TID (**t**ransversely **i**sotropic **d**ispersion).

(iii) Perfectly aligned fibers (no dispersion in either plane), as introduced in the HGO model in 2000, see Holzapfel et al. [26]. For this special case both concentration parameters (a, b) become infinite so that $\kappa_{\mathrm{op}} \to 1/2$. The structure tensors (5) are then $\mathbf{H}_i = \mathbf{M}_i \otimes \mathbf{M}_i$. This corresponds to $A = 0$, $B = 1$ in (5). We refer to this special case as PA (**p**erfect **a**lignment).

Figure 1 depicts a visualization of $\rho(\mathbf{N})\mathbf{N}$ (for just one family of fibers), where the unit vector $\mathbf{N}$ is an arbitrary fiber direction in the reference configuration, for (a) the general case for which $\mathbf{H}_i$ is given by (5), (b) the transversely isotropic dispersion (TID) with $\mathbf{H}_i$ given by (25) and (c), the case of perfect alignment (PA) of collagen fibers.

As mentioned above the fiber dispersions described in (ii) and (iii) are special cases of the non-rotationally symmetric dispersion model, which is considered to be the reference model. Subsequently, we use (material and structural) parameters for the media and adventitia of healthy abdominal aortas (median values) according to Niestrawska et al. [3]. The material parameters (c, k_1, k_2) were determined from biaxial stretching tests and adopted from Table 4 in [3], while the structural parameters (κ_{ip}, κ_{op}, α) were determined from second harmonic
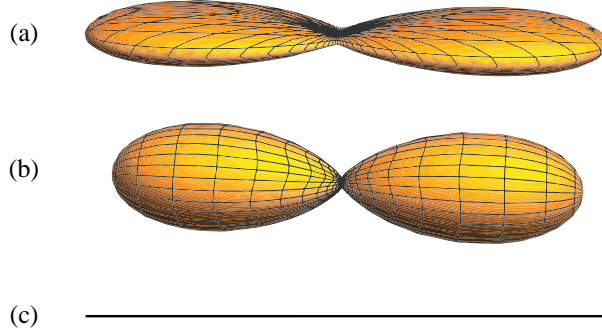
Figure 1: Visualization of three cases of fiber dispersions defined by $\rho(\mathbf{N})\mathbf{N}$, with $\rho = \rho_{\mathrm{ip}}\rho_{\mathrm{op}}$ according to (1), where the distance from the center to the surface represents the probability of finding a fiber in the direction $\mathbf{N}$: (a) non-rotationally symmetric dispersion (the general case); (b) transversely isotropic dispersion; (c) perfectly aligned fibers. The plots have been scaled differently.

	c (kPa)	k_1 (kPa)	k_2 (–)	κ_{ip} (–)	κ_{op} (–)	α (°)
Media	16.08	11.68	7.18	0.208	0.487	6.91
Adventitia	3.77	0.36	45.88	0.232	0.466	77.53
AAA	3.72	2.73	123.52	0.261	0.438	9.05

Table 1: Material parameters (c, k_1, k_2) from biaxial stretching tests and structural parameters (κ_{ip}, κ_{op}, α) from second harmonic generation images, for healthy medias and adventitias of human abdominal aortas (median values), and for one AAA wall sample; taken from Tables 2-5 of Niestrawska et al. [3].

generation images and adopted from Table 2 in [3]. In addition, we also use structural and material parameters from one AAA wall sample, and adopt the values from Tables 3 and 5 in [3], i.e. sample AAA-5. The parameters are summarized in Table 1. For the case of transversely isotropic dispersion we take $\kappa_{\mathrm{op}} = 0.414$, 0.406 for the media and adventitia of the healthy abdominal aorta, respectively, and 0.397 for the AAA wall. These values are calculated using the relationship $\kappa_{\mathrm{op}} = 1/2(1 + \kappa_{\mathrm{ip}})$, where κ_{ip} is taken from Table 1. This relationship results from the symmetry of the structure tensor (in-pane and out-of-plane dispersions are symmetric). From these values it is straightforward to determine the individual dispersion parameter κ and the corresponding constants A and B. Finally, for the perfectly aligned fibers we set $A = 0$, $B = 1$ ($\kappa_{\mathrm{op}} = 1/2$). These material and structural parameters are now taken for the subsequent three examples.
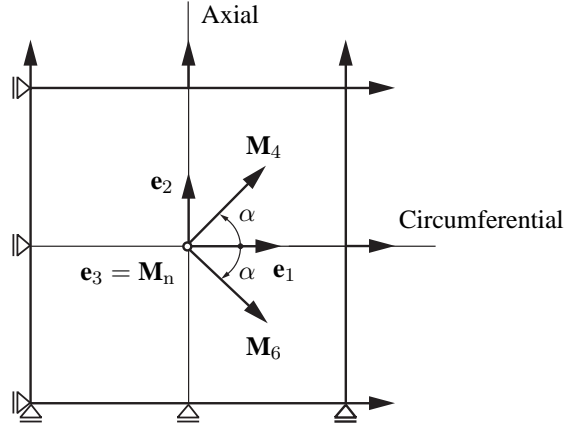
Figure 2: Cuboid-shaped sample of a healthy media (and a AAA wall) reinforced by two symmetric fiber families, denoted by $\mathbf{M}_4$ and $\mathbf{M}_6$, and subjected to equibiaxial extension within the $(\mathbf{e}_1, \mathbf{e}_2)$ plane.

3.2 Planar biaxial extension

On the basis of a planar equibiaxial extension test we study the three different cases of fiber dispersions, as discussed in the previous section. In particular, we consider samples of a healthy media and a AAA wall with the dimension $20 \times 20 \times 1.5\,\mathrm{mm}$, which resembles the geometry used for the actually performed biaxial extension experiments documented in [3].

Four hexahedral mixed $Q1$-$P0$ elements (constant pressure and trilinear displacement interpolations) are used for the discretization of a cuboid, which is reinforced by two symmetric fiber families located in the $(\mathbf{e}_1, \mathbf{e}_2)$ plane, see Fig. 2. The samples are subjected to equibiaxial extension within the $(\mathbf{e}_1, \mathbf{e}_2)$ plane up to a stretch of $\lambda_{\mathrm{circ}} = \lambda_{\mathrm{axial}} = 1.25$, using a displacement-driven analysis. The analytical solutions are calculated according to [4] using MATLAB [30] and compared with the finite element solutions computed by means of FEAP [29].

3.3 Inflation of residually stressed and pre-stretched aortic segments

Here we study the influence of the fiber dispersion on the mechanical response of residually stressed and pre-stretched (idealized) aortic segments. In particular, a healthy aorta consisting of media and adventitia, and an aneurysmatic abdominal aorta are analyzed.

3.3.1 Geometry

The wall thickness and axial length are chosen to be $1.5\,\mathrm{mm}$, whereas the initial inner radius R_i is $10\,\mathrm{mm}$. For the healthy aortic segment the thickness ratio of media/adventitia is chosen
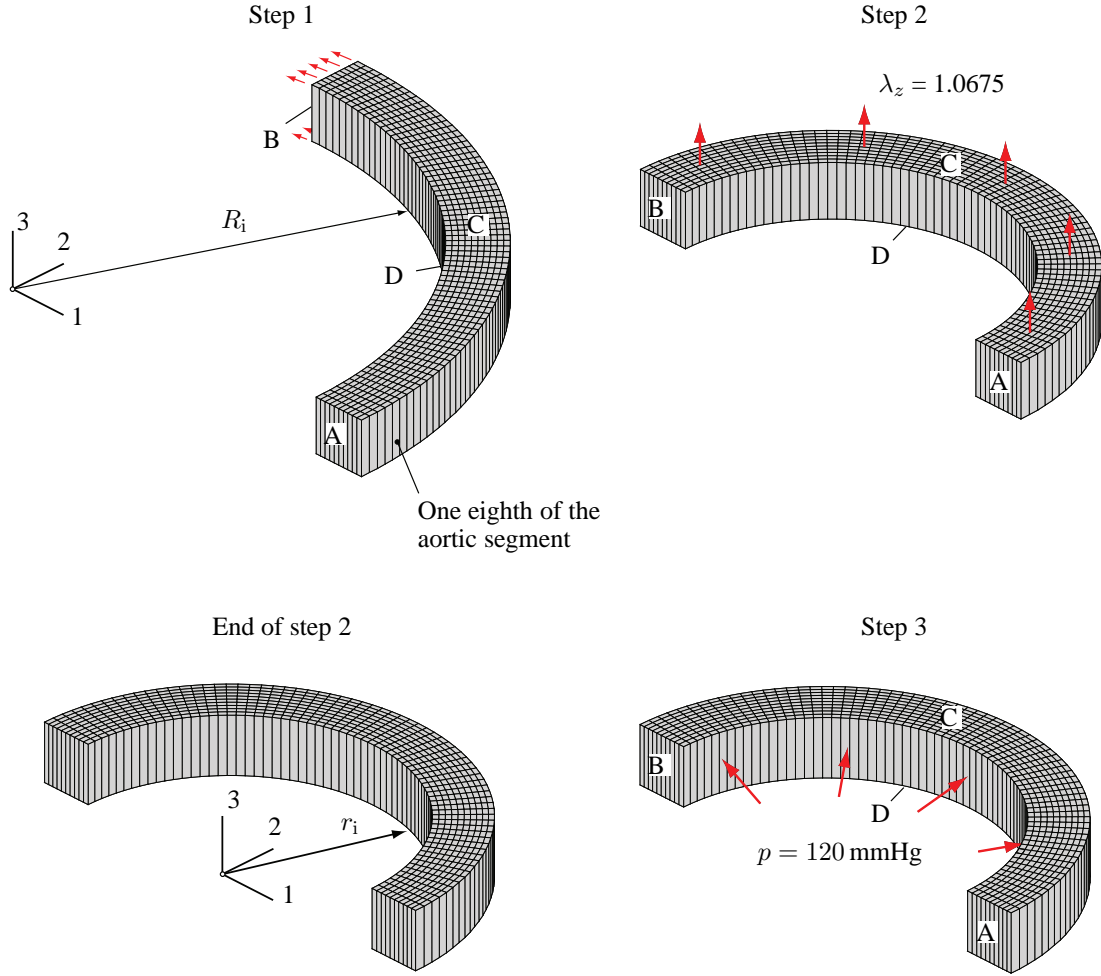
Figure 3: Three steps performed during the simulation of a residually stressed and pre-stressed (cylindrical) aortic segment. Due to symmetry one eighth of the segment is simulated. First, the opening angle of $180°$ ($90°$ because of symmetry) of the segment with inner radius R_i is closed; second, an axial pre-stretch of $\lambda_z = 1.0675$ is applied to obtain the inner radius r_i; third, the aortic segment is pressurized with an inner pressure p up to $120\,\mathrm{mmHg}$.

following the experimental findings of Schriefl et al. [2] and Niestrawska et al. [3], i.e. 70% of the wall thickness is occupied by the media, and 30% by the adventitia. The AAA segment is modeled as one single layer with $1.5\,\mathrm{mm}$ wall thickness. The initial (stress-free) geometry is a cylindrical segment cut open with an opening angle of $180°$ (defined according to Fig. 3 in [26]), which is slightly smaller than the opening angles reported for healthy abdominal aortas (Holzapfel et al. [31]; Greenwald [32]). For a better comparison of the material responses between healthy and diseased segments, and as there are no experimental data available on opening angles for aneurysmatic aortas, the same opening angle is chosen for both cases.

3.3.2 Finite element model

The geometry is discretized by one element in the axial direction, 70 elements in the circumferential direction and 10 in the radial direction. For the healthy aortic segment 7 elements are used for the media in the radial direction, and 3 for the adventitia.

Figure 3 shows the steps performed during the simulation. Due to symmetry, only one eighth of the aortic segment is simulated, therefore, the opening angle is $180°/2 = 90°$. In step 1 the segment is closed to form a quarter of the segment by constraining surface A in the 2 direction and surface B in both the 1 and 2 directions, and by applying the SPIN command in FEAP to surface B. This command rotates the selected nodes around the center and respective to a defined axis of rotation. Simultaneously, the lower surface D is restricted in the 3 direction. Then, the upper and lower surfaces C and D are restricted in the 3 direction and A and B are constrained in the 2 direction only. In step 2 the aortic segment is stretched by an axial pre-stretch λ_z of 1.0675, achieved by a displacement-driven loading on surface C (the pre-stretch is calculated for the corresponding age following the approach proposed by Horn et al. [33]). At the end of step 2 the inner radius r_i is taken for the normalization of subsequent plots. In step 3 (the last step) the boundary conditions are left unchanged with respect to step 2, and the aortic segment is inflated with an inner pressure p of 120 mmHg using a pressure boundary loading (pressure loads depend on the deformation).

3.4 Inflation of an idealized AAA geometry

The final example underlines the importance of using accurate fiber dispersions in AAA simulations. We are utilizing an idealized AAA geometry to study the effects of fiber dispersions on the mechanical AAA response in a repeatable way using a mathematical function for the AAA shape; therefore, a patient-specific geometry is deliberately not used. In this example we use again the material and structural parameters from Section 3.1, and, in addition, we analyze a fourth case, namely isotropic fiber dispersion which is represented by a uniform dispersion in each plane so that $\rho_{ip} = \rho_{op} = 1$, where the structure tensor is simply $(1/3)\mathbf{I}$. Hence, we have no preferred direction so that $\kappa = 1/3$ in (25), with $A = 1/3$ and $B = 0$ in (5).

3.4.1 Geometry

The idealized geometry of the AAA segment is generated using the toolkit CUBIT [34] and MATLAB [30]. The initial AAA thickness is chosen to be the same as in the example of Section 3.3, i.e. 1.5 mm. The (total) length L of the AAA model is 160 mm, while the AAA shape,

i.e. the change in the radius R, is defined by a 'parabolic-exponential shape' function proposed by Elger et al. [5], and utilized in, e.g., Rodríguez et al. [24]. Thus,

$$R(Z) = R_{\mathrm{a}} + \left(R_{\mathrm{an}} - R_{\mathrm{a}} - c_3 \frac{Z^2}{R_{\mathrm{a}}} \right) \exp \left(-c_2 \left| \frac{Z}{R_{\mathrm{a}}} \right|^{c_1} \right), \tag{26}$$

where Z denotes the axial coordinate, R_{a} is the radius of the healthy aorta (for the analyses we use $R_{\mathrm{a}} = 15\,\mathrm{mm}$), R_{an} is the maximum radius of the aneurysm (at $Z = 0$), $c_1 = 0.5$ is a constant and c_2 and c_3 are defined as

$$c_2 = \frac{4.605}{(0.5 L_{\mathrm{an}}/R_{\mathrm{a}})^{c_1}}, \qquad c_3 = \frac{R_{\mathrm{an}} - R_{\mathrm{a}}}{R_{\mathrm{a}}(0.8 L_{\mathrm{an}}/R_{\mathrm{a}})^2}, \tag{27}$$

where L_{an} is the length of the aneurysm (Rodríguez et al. [24]). For a sketch of one eighth of the AAA geometry see Fig. 4. Following [24] we us the dimensionless geometrical parameters

$$F_{\mathrm{R}} = \frac{R_{\mathrm{an}}}{R_{\mathrm{a}}}, \qquad F_{\mathrm{L}} = \frac{L_{\mathrm{an}}}{R_{\mathrm{an}}}, \tag{28}$$

where F_{R} is the ratio between the AAA radius and the radius of the healthy aorta, and F_{L} is the ratio between the length of the aneurysm L_{an}, and the maximum AAA radius; we use $F_{\mathrm{R}} = 2.5$ and $F_{\mathrm{L}} = 2.8$.

3.4.2 Finite element model

The 3D geometry is discretized with CUBIT, and the analysis is performed with FEAP using $1\,488$ hexahedral mixed $Q1$-$P0$ elements. An inner pressure of $16\,\mathrm{kPa}$ ($\sim 120\,\mathrm{mmHg}$) is applied to simulate the mean blood pressure. Symmetric boundary conditions are employed allowing the simulation of only one eighth of the idealized AAA geometry, which reduces the computational time significantly. The axial direction is restricted on both outlets, see Fig. 4.

3.4.3 Definition of fiber orientation

In order to include the fiber orientation, the local circumferential, axial and radial vectors of a finite element, say $\mathbf{e}_1^{\mathrm{local}}$, $\mathbf{e}_2^{\mathrm{local}}$, $\mathbf{e}_3^{\mathrm{local}}$, need to be identified. This task is straightforward for a cylindrical geometry but it is more elaborate for a AAA geometry, where the local axial direction varies as well. We include the fiber dispersion by using a local coordinate system for each individual finite element. Three nodes on the upper (top) surface and three nodes on the lower (bottom) surface of an individual element are used to define two planes. Hence, two orthogonal vectors to these planes can be identified, i.e. $\mathbf{e}_3^{\mathrm{top}}$ and $\mathbf{e}_3^{\mathrm{bottom}}$, see Fig. 5. Consequently, we
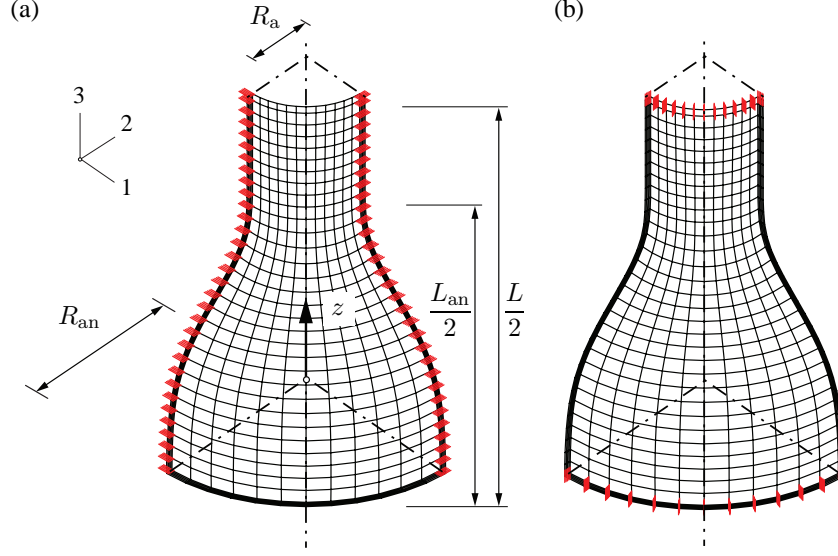
13

Figure 4: One eighth of the idealized AAA geometry and applied boundary conditions in (a) along the directions 1 and 2, and (b) along the direction 3; L is the (total) length of the AAA model, L_an is the length of the aneurysmatic part, R_a is the radius of the healthy aorta (at $Z = 0$), R_an is the maximum radius of the aneurysm (at $Z = L/2$), while Z denotes the local axial coordinate, see Elger et al. (27).

define the local radial (unit) vector as

$$\mathbf{e}_3^\text{local} = \frac{\mathbf{e}_3^\text{top} + \mathbf{e}_3^\text{bottom}}{|| \, \mathbf{e}_3^\text{top} + \mathbf{e}_3^\text{bottom} \, ||}. \tag{29}$$

Subsequently, the local circumferential vector $\mathbf{e}_1^\text{local}$ is calculated by using the cross product of the global axial vector $\mathbf{e}_2$ and the calculated local radial vector $\mathbf{e}_3^\text{local}$, i.e.

$$\mathbf{e}_1^\text{local} = \mathbf{e}_2 \times \mathbf{e}_3^\text{local}. \tag{30}$$

Finally, the local axial vector $\mathbf{e}_2^\text{local}$ is calculated as

$$\mathbf{e}_2^\text{local} = \mathbf{e}_3^\text{local} \times \mathbf{e}_1^\text{local}. \tag{31}$$

By utilizing the local coordinate system the mean fiber directions, as introduced in Section 2.2, are then determined as

$$\mathbf{M}_4 = \cos\alpha\mathbf{e}_1^\text{local} + \sin\alpha\mathbf{e}_2^\text{local}, \qquad \mathbf{M}_6 = \cos\alpha\mathbf{e}_1^\text{local} - \sin\alpha\mathbf{e}_2^\text{local}, \tag{32}$$
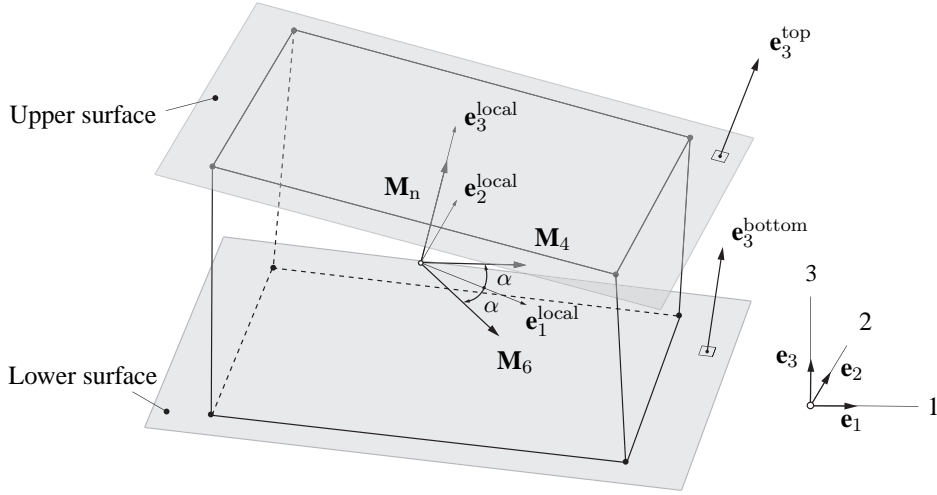
and $\mathbf{M}_\text{n} = \mathbf{e}_3^\text{local}$.

14

Figure 5: Local vectors $\mathbf{e}_1^{\mathrm{local}}$, $\mathbf{e}_2^{\mathrm{local}}$, $\mathbf{e}_3^{\mathrm{local}}$ required for the definition of the local fiber orientations within an individual finite element.

4   Simulation Results and Discussion

This section documents the numerical results of the systematically performed simulations of the three representative examples according to Section 3, and it provides short discussions.

4.1   Planar biaxial extension

Figure 6 displays plots for the Cauchy stress (σ_{circ}, σ_{axial}) versus the related stretch (λ_{circ}, λ_{axial}) for a sample of the healthy media and one for the AAA wall considering the fiber dispersions NRSD, TID and PA. The numerical (FE) and the analytical results coincide very well, which indicates the correct implementation of the material model into FEAP [29]. As can be seen, the fiber dispersion has a significant influence on the mechanical behavior of the samples.

Images indicate that collagen fibers exhibit a very small out-of-plane dispersion for the healthy media but a significant in-plane dispersion (Schriefl et al. [35]; Niestrawska et al. [3]). TID assumes too little in-plane fibers leading to a weaker material response in both circumferential and axial direction compared with NRSD, see Fig. 6(a). If PA is used (with $\alpha = 6.91°$) then too many fibers reinforce the circumferential direction, therefore, a PA of fibers overestimates the stiffness in the circumferential direction and underestimates it in the axial direction when compared with NRSD. The nonlinear stiffening in the axial direction can only be captured with the use of NRSD. Table 2 summarizes the Cauchy stresses (in kPa) at 1.15 and 1.20 stretch. Stresses in the circumferential direction at 1.20 stretch for PA of fibers are overesti-
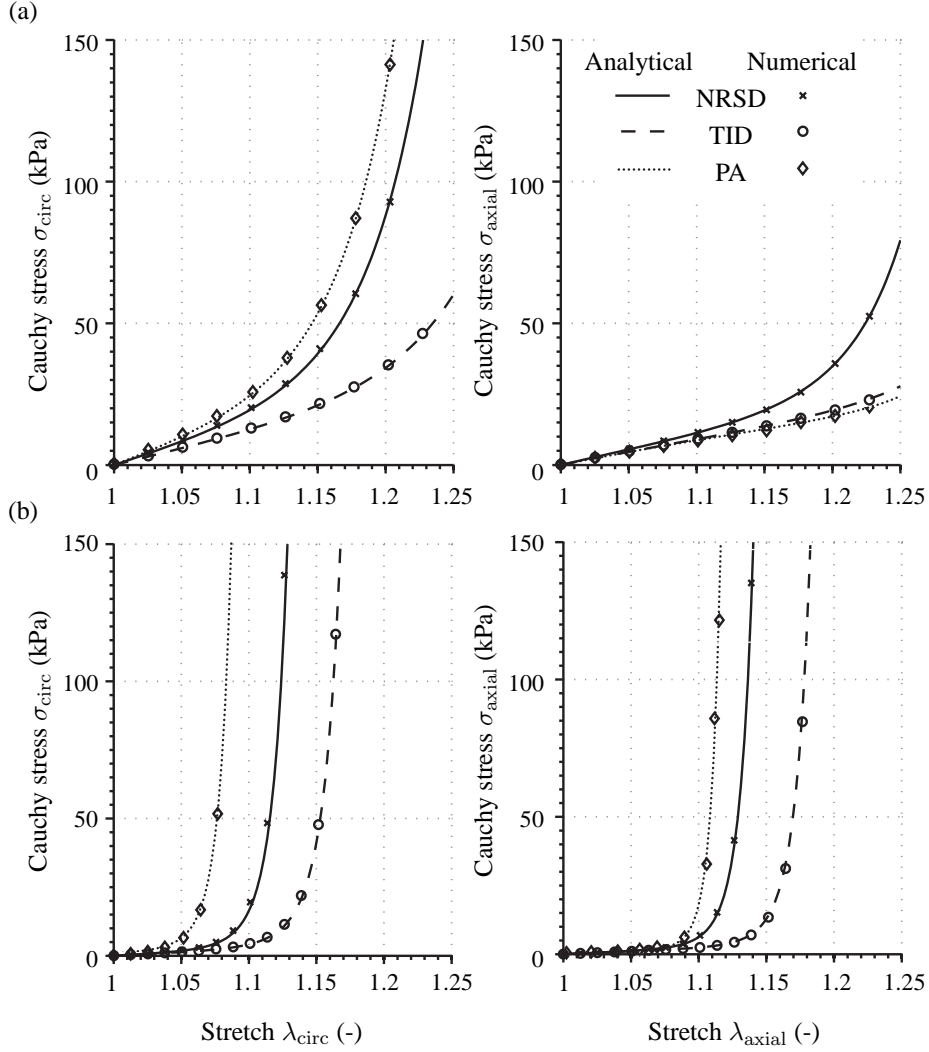
Figure 6: Planar equibiaxial extension of a cuboid-shaped sample to examine the difference in the mechanical behavior due to non-rotationally symmetric dispersion (NRSD), transversely isotropic dispersion (TID) and perfect alignment (PA) of fibers. Analytical and numerical (FE) solutions are compared: (a) healthy media, (b) AAA wall.

mated by 52% compared with NRSD, whereas the axial Cauchy stress is underestimated by 56%. The TID underestimates both circumferential and axial Cauchy stresses by 62% and 45%, respectively.

A similar tendency can be seen for the AAA sample, although the out-of-plane dispersion of fibers is (much) higher for AAAs compared with healthy tissues. Especially when stresses are compared at stretches of 1.05 and 1.10 the differences become clear, see Table 2. The analysis based on PA of fibers shows a faster stiffness when compared with TID and NRSD. At $\lambda_{circ} = 1.05$ the related stress is already 327% higher compared with NRSD, and at $\lambda_{circ} = 1.10$ the circumferential Cauchy stress is about 45 times higher for PA with respect to NRSD.

HEALTHY MEDIA					
	Circumferential		Axial		
Stretch λ	1.15	1.20	1.15	1.20	
	41.06	92.92	19.50	35.23	NRSD
Stress σ	21.68	35.39	13.84	19.37	TID
	56.36	141.10	12.25	15.57	PA

AAA WALL					
	Circumferential		Axial		
Stretch λ	1.15	1.20	1.15	1.20	
	1.99	19.54	1.31	6.84	NRSD
Stress σ	1.42	4.47	1.13	2.49	TID
	6.51	879.9	1.14	10.87	PA

Table 2: Cauchy stresses σ (in kPa) at two stretches λ (in the circumferential and axial directions) of the equibiaxially loaded cuboid-shaped sample for NRSD, TID and PA of fibers, for the healthy media and the AAA wall.

4.2   Inflation of residually stressed and pre-stretched aortic segments

Figure 7 illustrates the thickness change of the aortic wall with respect to the inner pressure p for the healthy aortic and AAA segments. Initial thickness, at $p = 0$, is with respect to the configuration 'end of step 2', as marked in Fig. 3. The closing of the open segments results in different wall thicknesses before inflation. For the AAA segment the wall thicknesses at $p = 0$ are quite dependent on the used fiber-reinforcement (see Fig. 7(b)), because the AAA segment is much stiffer than the healthy aortic segment. As can be seen, the choice of the fiber dispersion is strongly influencing the results. For both investigated segments the analyses with PA of fibers provide (by far) the stiffest response, resulting in a 5.6% smaller wall thickness at $120\,\mathrm{mmHg}$ when compared with NRSD for the AAA segment. On the other hand the segments with TID show the most compliant responses, while the mechanical responses with NRSD are in between. The difference of the material behavior between the two segments (healthy aorta versus AAA) is as pronounced as already shown in Section 4.1.

Figure 8 depicts 3D plots of the circumferential and axial Cauchy stresses versus the inner pressure and the normalized radius for the AAA segment, and compares the influence of the three different dispersion assumptions. The current radius is here normalized with the inner radius r_i, as depicted in the configuration 'end of step 2' of Fig. 3. Especially, the circumferential
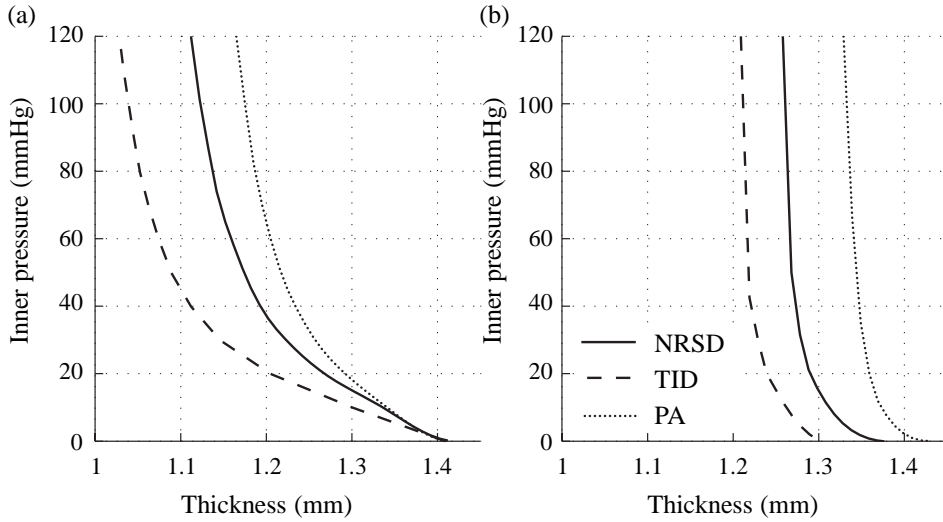
17

Figure 7: FE results of wall thickness versus inner pressure for (a) the healthy aortic segment and (b) the AAA wall using three different fiber dispersions: non-rotationally symmetric dispersion (NRSD), transversely isotropic dispersion (TID), perfect alignment (PA) of fibers.
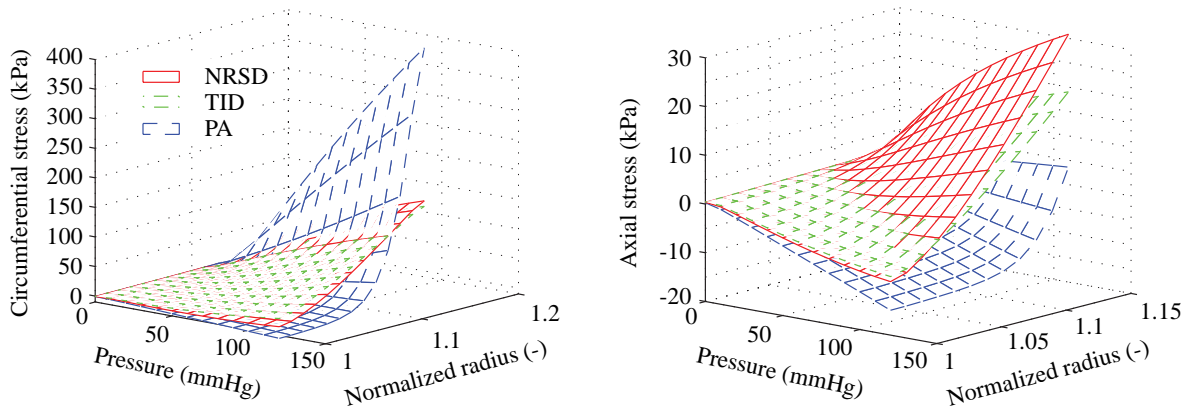

Figure 8: FE results of circumferential and axial Cauchy stresses versus normalized radius and inner pressure for the AAA segment with three different fiber dispersions: non-rotationally symmetric dispersion (NRSD), transversely isotropic dispersion (TID), perfect alignment (PA) of fibers.

and axial Cauchy stresses analyzed on the basis of PA of fibers are significantly different with respect to the other two fiber dispersions, with a peak circumferential (Cauchy) stress of over $300\,\mathrm{kPa}$.

Figure 9 depicts the distributions of the circumferential Cauchy stresses with respect to the geometry at $120\,\mathrm{mmHg}$. Clearly, wall thicknesses and radii differ between the healthy and aneurysmatic segments, and also between the different fiber dispersions.
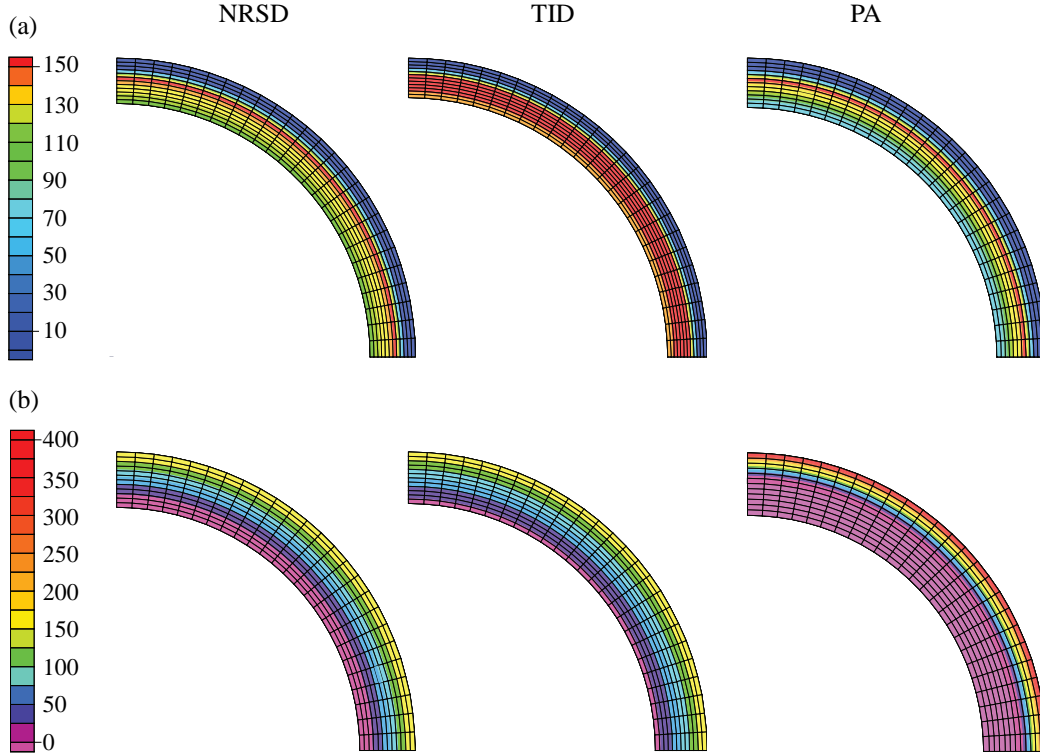
Figure 9: FE results of the circumferential Cauchy stress distributions (in kPa) at $120\,\mathrm{mmHg}$ for (a) the healthy aortic segment and (b) the AAA segment using three different fiber dispersions: non-rotationally symmetric dispersion (NRSD), transversely isotropic dispersion (TID), perfect alignment (PA) of fibers. Note the different scales for the stress in (a) and (b).

4.3 Inflation of an idealized AAA geometry

Figure 10 shows circumferential and axial Cauchy stresses versus the (current) inner radius for different fiber dispersions up to $120\,\mathrm{mmHg}$ for (a) the cylindrical segment (healthy aorta) at the smallest radius (at $Z = L/2$), and (b) at the maximum radius of the bulged AAA segment (at $Z = 0$). All simulations except for the one which considers isotropic dispersion show compressive axial stresses in the cylindrical (healthy) part of the aorta, which occur due to the boundary conditions. In addition, the circumferential stresses are higher with isotropic dispersion, labeled as ISO, as they are with NRSD and TID. The cylindrical segment with the smallest radius and the maximum radius of the bulged AAA segment (with ISO) exhibits the largest radial extension (with a value of $53.54\,\mathrm{mm}$ at $120\,\mathrm{mmHg}$), not having enough fibers located in the circumferential direction to prevent excessive extension due to the applied pressure. TID exhibits a more compliant behavior in the diseased region (with respect to NRSD) with a maximal circumferential stress of $760.7\,\mathrm{kPa}$, whereas NRSD reaches $674.2\,\mathrm{kPa}$ at a maximal inner
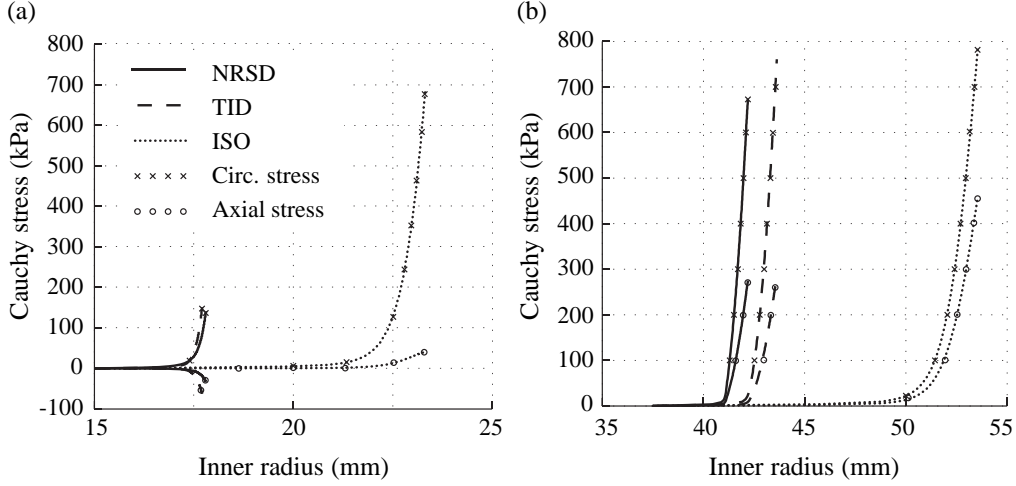
Figure 10: Circumferential and axial Cauchy stresses versus (current) inner radius up to $120\,\mathrm{mmHg}$ for (a) the cylindrical segment (healthy aorta) at the smallest radius (at $Z = L/2$) and (b) at the maximum radius of the bulged AAA segment (at $Z = 0$). Three different fiber dispersions are investigated: non-rotationally symmetric dispersion (NRSD), transversely isotropic dispersion (TID), isotropic (ISO).

radius of $42.9\,\mathrm{mm}$. Note that no solutions for the AAA with PA of fibers can be displayed, as this case showed numerical instabilities at higher pressure levels in the neck region. This is most likely due to the significant differences in stiffness between the compliant ground matrix and the (relatively) stiff fibers. As there is no fiber dispersion and the fibers are located close to the circumferential direction numerical instabilities occur, which may arise due to the used isochoric-volumetric split of the strain-energy function (see, e.g., Helfenstein et al. [36]).

Figure 11 shows circumferential and axial Cauchy stresses as a function of the radius r normalized with R_{an} for different assumptions of fiber dispersions. The analysis on the basis of an isotropic dispersion predicts axial stresses almost twice as high as for TID and NRSD. The prediction of circumferential stresses obtained on the basis of TID is higher than those using NRSD throughout the wall thickness.

Figure 12(a) shows contour plots of the circumferential Cauchy stress for the three simulations at $120\,\mathrm{mmHg}$. The scale of the stress is the same for all simulations. In Fig. 12(b) the stress scale is changed so that the location of the maximal stress is visible in the ISO stress plot. All three analyses reveal that the peak wall stress is located at the luminal side of the AAA. The peak circumferential stress (which was almost identical with the maximal principal stresses) occurs at the maximum diameter except for ISO, where the maximum stress is located at the transition zone (compare with Fig. 12), hence an isotropic model is inappropriate for this type
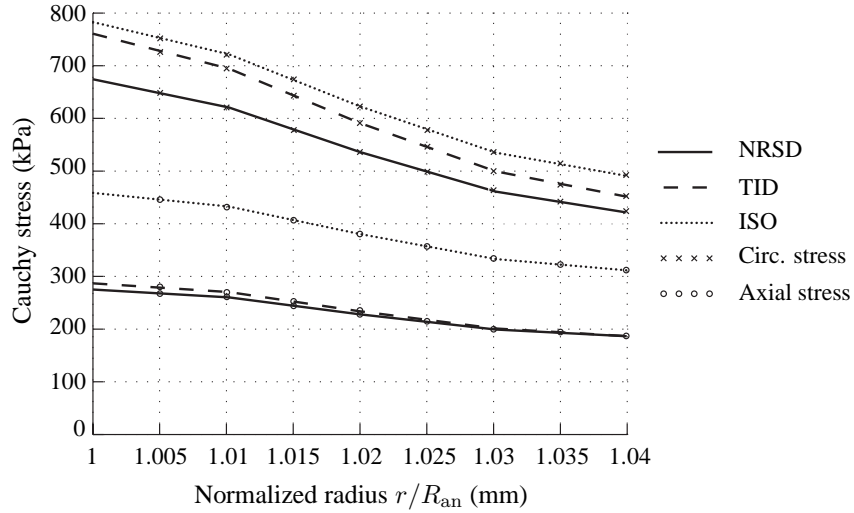
20

Figure 11: Circumferential and axial Cauchy stresses versus normalized radius r/R_{an} for three different assumptions of fiber dispersions: non-rotationally symmetric dispersion (NRSD), transversely isotropic dispersion (TID), isotropic (ISO).
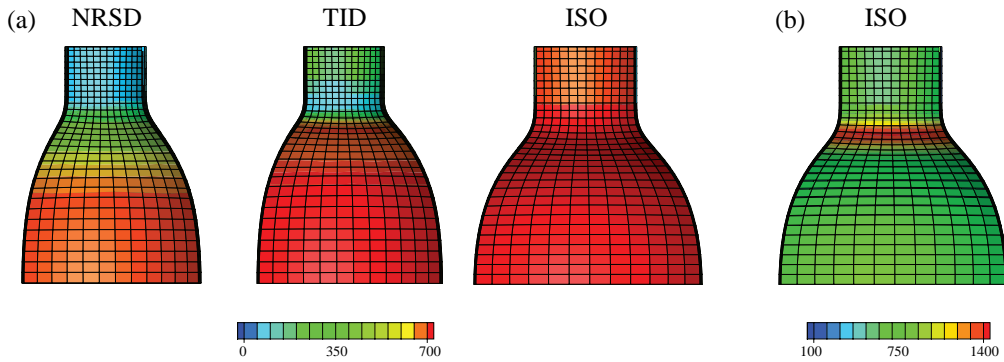

Figure 12: Contour plots of the circumferential Cauchy stress (in kPa) on the luminal side at 120 mmHg: (a) three different assumptions of fiber dispersions (using the same scale), i.e. non-rotationally symmetric dispersion (NRSD), transversely isotropic dispersion (TID), isotropic (ISO); (b) stress plot for the case ISO with a stress scale which makes the location of the peak wall stress in the transitional zone visible.

of analysis. The stress distributions between the cases NRSD and TID are not as pronounced as with respect to ISO, because AAA tissues exhibit a rather large out-of-plane dispersion, closer to a rotationally symmetric dispersion, than it is the case for healthy aortas.

Previous studies detected peak wall stresses at inflection points and a pronounced influence of asymmetry on the location of the peak wall stress (Vorp et al. [6]; Doyle et al. [39, 40]; Rodríguez et al. [24]). Interestingly, in the present example only the isotropic model exhibits peak wall stresses at the inflection point. Rodríguez et al. [25] demonstrated that an anisotropic

model yields much higher wall stresses when compared with an isotropic model; the authors also discussed the influence of fiber dispersion. However, the models the authors used are not comparable, as they fitted their models to different data sets, using different fitting procedures. The present simulation of an idealized AAA geometry shows twice as high maximal stresses for the isotropic case compared to the anisotropic cases. As the used structural and material parameters are not comparable with the ones used by Rodríguez et al. [25] the differences in the findings highlight the influence of parameters and model assumptions on stress magnitudes and locations.

5 Conclusion

The influence of different fiber dispersions on the mechanical response of aortic tissues in health and disease has not yet been studied on the basis of the recent constitutive model of Holzapfel et al. [4]. In the present study we have performed a systematic analysis using three representative numerical examples. Magnitudes and distributions of stresses and deformations were presented and discussed. We have used structural and mechanical data from human aortic samples (healthy media/adventitia and AAA), recently documented by Niestrawska et al. [3].

Simulations performed with data from healthy aortas show a (more) gradual stiffening, whereas the simulations with AAA data predict a very compliant response at low stretches, then a kind of 'stiffening point' at which a rapid stiffening of the material response occurs. For that stiffening the collagen micro-structure is mainly responsible. Therefore, for AAA tissues it is even more important to consider the corresponding fiber dispersion. In all three examples it is visible that structural and material data from healthy aortic tissues yield a (completely) different material response when compared with AAA tissue. Consequently, data from healthy tissues should not be used for the prediction of peak wall stresses in AAAs, or *vice versa*.

All simulations show a rather remarkable influence of the fiber dispersion on the magnitudes and distributions of stresses and deformations. The most severe difference can be appreciated in the example analyzing the inflation of an idealized AAA geometry. For example, the peak circumferential stress is more than twice as high with isotropic dispersion compared with non-rotationally symmetric dispersion, and even the related location of the peak stress is different. The computational study indicates that small changes in the fiber dispersion result in a rather different tissue behavior. Hence, as long as structural parameters are available they should be considered in the analysis, especially as the computational time is about the same for different arterial micro-structures. Clearly, it is not sufficient to use phenomenological models to

understand disease progression.

Future studies should focus on the inclusion of new imaging data of the micro-structure. Intermediate stages of AAA formation should also be studied on, e.g., mouse models to provide data for more detailed micro-structural modeling and analyses. Another key research topic is certainly the collection of structural data *in vivo*, which would help to establish more realistic rupture criteria, and to better understand collagen reorientation during disease progression.

References

[1] G. A. Holzapfel and R. W. Ogden. Constitutive modelling of passive myocardium: a structurally based framework for material characterization. *Phil. Trans. R. Soc. Lond. A*, 367:3445–3475, 2009.

[2] A. J. Schriefl, G. Zeindlinger, D. M. Pierce, P. Regitnig, and G. A. Holzapfel. Determination of the layer-specific distributed collagen fiber orientations in human thoracic and abdominal aortas and common iliac arteries. *J. R. Soc. Interface*, 9:1275–1286, 2012.

[3] J. A. Niestrawska, Ch. Viertler, P. Regitnig, T. U. Cohnert, G. Sommer, and G. A. Holzapfel. Microstructure and mechanics of healthy and aneurysmatic abdominal aortas: experimental analysis and modeling. *J. R. Soc. Interface*, 13:20160620, 2016.

[4] G. A. Holzapfel, J. A. Niestrawska, R. W. Ogden, A. J. Reinisch, and A. J. Schriefl. Modelling non-symmetric collagen fibre dispersion in arterial walls. *J. R. Soc. Interface*, 12:20150188, 2015.

[5] D. F. Elger, R. S. Blackketter, R. S. Budwig, and K. H. Johansen. The influence of shape on the stresses in model abdominal aortic aneurysms. *J. Biomed. Eng.*, 118:326–332, 1996.

[6] D. A. Vorp, M. L. Raghavan, and M. W. Webster. Mechanical wall stress in abdominal aortic aneurysm: Influence of diameter and asymmetry. *J. Vasc. Surg.*, 27:632–639, 1998.

[7] M. L. Raghavan, D. A. Vorp, M. P. Federle, M. S. Makaroun, and M. W. Webster. Wall stress distribution on three-dimensionally reconstructed models of human abdominal aortic aneurysm. *J. Vasc. Surg.*, 31:760–769, 2000.

[8] M. L. Raghavan and D. A. Vorp. Toward a biomechanical tool to evaluate rupture potential of abdominal aortic aneurysm: identification of a finite strain constitutive model and evaluation of its applicability. *J. Biomech.*, 33:475–482, 2000.

[9] M. J. Thubrikar, J. Al-Soudi, and F. Robicsek. Wall stress studies of abdominal aortic aneurysm in a clinical model. *Ann. Vasc. Surg.*, 15:355–366, 2001.

[10] B. J. Doyle, A. J. Cloonan, M. T. Walsh, D. A. Vorp, and T. M. McGloughlin. Identification of rupture locations in patient-specific abdominal aortic aneurysms using experimental and computational techniques. *J. Biomech.*, 43:1408–1416, 2010.

[11] S. S. Raut, A. Jana, V. De Oliveira, S. C. Muluk, and E. A. Finol. The effect of uncertainty in vascular wall material properties on abdominal aortic aneurysm wall mechanics. In B. Doyle, K. Miller, A. Wittek, and P. M. F. Nielsen, editors, *Computational Biomechanics for Medicine. Fundamental Science and Patient-specific Applications*, pages 69–86. Springer, New York, 2014.

[12] D. M. Pierce, T. E. Fastl, B. Rodriguez-Vila, P. Verbrugghe, I. Fourneau, G. Maleux, P. Herijgers, E. J. Gomez, and G. A. Holzapfel. A method for incorporating three-dimensional residual stretches/stresses into patient-specific finite element simulations of arteries. *J. Mech. Behav. Biomed. Mater.*, 47:147–164, 2015.

[13] M. M. Stringfellow, P. F. Lawrence, and R. G. Stringfellow. The influence of aorta-aneurysm geometry upon stress in the aneurysm wall. *J. Surg. Res.*, 42:425–433, 1987.

[14] D. C. McGiffin, P. B. McGiffin, A. J. Galbraith, and R. B. Cross. Aortic wall stress profile after repair of coarctation of the aorta. It is related to subsequent true aneurysm formation? *J. Thorac. Cardiovasc. Surg.*, 104:924–931, 1992.

[15] F. Inzoli, F. Boschetti, M. Zappa, T. Longo, and R. Fumero. Biomechanical factors in abdominal aortic aneurysm rupture. *Eur. J. Vasc. Surg.*, 7:667–674, 1993.

[16] W. R. Mower, L. J. Baraff, and J. Sneyd. Stress distributions in vascular aneurysms: factors affecting risk of aneurysm rupture. *J. Surg. Res.*, 55:155–161, 1993.

[17] J. P. Vande Geest, M. S. Sacks, and D. A. Vorp. The effects of aneurysm on the biaxial mechanical behavior of human abdominal aorta. *J. Biomech.*, 39:1324–1334, 2006.

[18] J. Tong, T. Cohnert, P. Regitnig, and G. A. Holzapfel. Effects of age on the elastic properties of the intraluminal thrombus and the thrombus-covered wall in abdominal aortic aneurysms: biaxial extension behavior and material modeling. *Eur. J. Vasc. Endovasc. Surg.*, 42:207–219, 2011.

[19] S. A. O'Leary, D. A. Healey, E. G. Kavanagh, M. T. Walsh, T. M. McGloughlin, and B. J. Doyle. The biaxial biomechanical behavior of abdominal aortic aneurysm tissue. *Ann. Biomed. Eng.*, 42:2440–2450, 2014.

[20] S. G. Sassani, J. Kakisis, S. Tsangaris, and D. P. Sokolis. Layer-dependent wall properties of abdominal aortic aneurysms: Experimental study and material characterization. *J. Mech. Behav. Biomed. Mater.*, 49:141–161, 2015.

[21] M. F. Fillinger, M. L. Raghavan, S. P. Marra, J. L. Cronenwett, and F. E. Kennedy. In vivo analysis of mechanical wall stress and abdominal aortic aneurysm rupture risk. *J. Vasc. Surg.*, 36:589–597, 2002.

[22] M. F. Fillinger, S. P. Marra, M. L. Raghavan, and F. E. Kennedy. Prediction of rupture risk in abdominal aortic aneurysm during observation: wall stress versus diameter. *J. Vasc. Surg.*, 37:724–732, 2003.

[23] S. Polzer, C. T. Gasser, J. Bursa, R. Staffa, R. Vlachovsky, V. Man, and P. Skacel. Importance of material model in wall stress prediction in abdominal aortic aneurysms. *Med. Eng. Phys.*, 35:1282–1289, 2013.

[24] J. F. Rodríguez, C. Ruiz, M. Doblaré, and G. A. Holzapfel. Mechanical stresses in abdominal aortic aneurysms: influence of diameter, asymmetry and material anisotropy. *J. Biomech. Eng.*, 130:021023–1–10, 2008.

[25] J. F. Rodríguez, G. Martufi, M. Doblaré, and E. A. Finol. The effect of material model formulation in the stress analysis of abdominal aortic aneurysms. *Ann. Biomed. Eng.*, 37: 2218–2221, 2009.

[26] G. A. Holzapfel, T. C. Gasser, and R. W. Ogden. A new constitutive framework for arterial wall mechanics and a comparative study of material models. *J. Elasticity*, 61:1–48, 2000.

[27] T. C. Gasser, R. W. Ogden, and G. A. Holzapfel. Hyperelastic modelling of arterial layers with distributed collagen fibre orientations. *J. R. Soc. Interface*, 3:15–35, 2006.

[28] G. A. Holzapfel. *Nonlinear Solid Mechanics. A Continuum Approach for Engineering*. John Wiley & Sons, Chichester, 2000.

[29] R. L. Taylor. *FEAP – A Finite Element Analysis Program, Version 8.4 User Manual*. University of California at Berkeley, Berkeley, California, 2013.

[30] MATLAB. R2016a, The MathWorks Inc., Natick, MA, USA, 2016.

[31] G. A. Holzapfel, G. Sommer, M. Auer, P. Regitnig, and R. W. Ogden. Layer-specific 3D residual deformations of human aortas with non-atherosclerotic intimal thickening. *Ann. Biomed. Eng.*, 35:530–545, 2007.

[32] S. E. Greenwald, J. E. Moore, Jr., A. Rachev, T. P. C. Kane, and J.-J. Meister. Experimental investigation of the distribution of residual strains in the artery wall. *J. Biomech. Eng.*, 119: 438–444, 1997.

[33] L. Horný, M. Netušil, and T. Voňavková. Axial prestretch and circumferential distensibility in biomechanics of abdominal aorta. *Biomech. Model. Mechanobiol.*, 13:783–799, 2014.

[34] A. B. Cubit. *Cubit 15.0 User Documentation*. Sandia National Laboratories, Albuquerque, New Mexico, USA, 2017.

[35] A. J. Schriefl, A. J. Reinisch, S. Sankaran, D. M. Pierce, and G. A. Holzapfel. Quantitative assessment of collagen fiber orientations from 2D images of soft biological tissues. *J. R. Soc. Interface*, 9:3081–3093, 2012.

[36] J. Helfenstein, M. Jabareen, E. Mazza, and S. Govindjee. On non-pyhsical response in models for fiber-reinforced hyperelastic materials. *Int. J. Solids Structures*, 47:2056–2061, 2010.

[37] J. A. Phillippi, S. Pasta, and D. A. Vorp. Biomechanics and pathobiology of aortic aneurysms. In T. McGloughlin, editor, *Biomechanics and Mechanobiology of Aneurysms*, pages 67–118. Springer, Heidelberg, 2011.

[38] D. Mohan and J. W. Melvin. Failure properties of passive human aortic tissue. II – biaxial tension tests. *J. Biomech.*, 16:31–44, 1983.

[39] B. J. Doyle, A. Callanan, and T. M. McGloughlin. A comparison of modelling techniques for computing wall stress in abdominal aortic aneurysms. *Biomed. Eng. Online*, 6:137–161, 2007.

[40] B. J. Doyle, A. Callanan, P. E. Burke, P. A. Grace, M. T. Walsh, D. A. Vorp, and T. M. McGloughlin. Vessel asymmetry as an additional diagnostic tool in the assessment of abdominal aortic aneurysms. *J. Vasc. Surg.*, 49:443–454, 2009.

[41] C. M. Scotti, J. Jimenez, S. C. Muluk, and E. A. Finol. Wall stress and flow dynamics in abdominal aortic aneurysms: finite element analysis vs. fluid–structure interaction. *Comput. Methods Biomech. Biomed. Engin.*, 11:301–322, 2008.